CFD Modeling of the Refining Process in an Industry-Scale Electric Arc Furnace: Analysis of Decarburization Efficiency and Model Validation



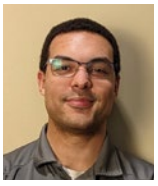


In the electric arc furnace (EAF) refining operation, molten steel is exposed to chemical-physical processes that modify the temperature and composition of the liquid bath to obtain the desired steel grades. These processes are controlled by gradients of flow velocity, temperature and composition that determine the rates of the refining reactions. By increasing flow mixing, it is possible to enhance the refining reactions and, consequently, to reduce the refining time and energy consumption. A computational fluid dynamics (CFD) solver developed to compute the refining stage in industrial-scale EAFs is applied to an EAF provided by EVRAZ. The CFD results are first compared with industry data obtained by EVRAZ for validation purposes, showing that the CFD prediction of carbon reduction during refining differs 1.7% from industry data. The validated model is then used to assess the impact of oxygen injection on decarburization efficiency.

Authors

Orlando Ugarte (top left), Research Scientist, Center for Innovation Through Visualization and Simulation and Steel Manufacturing Simulation and Visualization Consortium, Purdue University Northwest, Hammond, Ind., USA
ougarte@pnw.edu

Neel Busa, Center for Innovation Through Visualization and Simulation and Steel Manufacturing Simulation and Visualization Consortium, Purdue University Northwest, Hammond, Ind., USA

Bikram Konar (top right), EVRAZ North America, Regina, Sask., Canada

Sathvika Kottapalli, Center for Innovation Through Visualization and Simulation and Steel Manufacturing Simulation and Visualization Consortium, Purdue University Northwest, Hammond, Ind., USA

Tyamo Okosun (bottom left), Research Associate Professor, Center for Innovation Through Visualization and Simulation and Steel Manufacturing Simulation and Visualization Consortium, Purdue University Northwest, Hammond, Ind., USA

Chenn Q. Zhou (bottom right), NIPSCO Distinguished Professor of Engineering Simulation; Director, Center for Innovation Through Visualization and Simulation; Director, Steel Manufacturing Simulation and Visualization Consortium; Purdue University Northwest, Hammond, Ind., USA

Introduction

The electric arc furnace (EAF) is a steelmaking route that is widely adopted across the world. Its popularity has been growing in recent decades due to the low carbon emissions it generates as compared to the blast furnace–basic oxygen furnace (BOF) route,[1,2] and for the operation flexibility and high efficiency of the EAF process. The EAF operation facilitates the control of steel temperature and grade, which makes it suitable for the production of multiple steel products. The EAF uses electrical and chemical energy to melt and refine scrap charges to produce steel. In modern EAF operation, electrical energy accounts for 50–60% of the energy supplied to EAF.

It is possible to identify four stages during a typical EAF operation: charging, preheating, melting and refining. During the preheating stage, the temperature of the charged material is increased in order to facilitate the melting of the charge. During the melting stage, electrical and chemical heating (due to oxidation reactions and burners) are applied to the ferrous charge, leading to the melting of the charge and the formation of a molten bath. In the refining stage, chemical-physical processes are applied to the molten bath to obtain the desired chemistry and temperature of the liquid steel.

During the refining stage, the reactions are controlled by local concentration of species and thermodynamic variables, which are controlled by the flow field developed in the liquid steel. Therefore, it is possible to increase the reaction rates and facilitate the refining process by increasing the stirring of the molten bath. A number of technologies are applied to increase the stirring of molten steel during refining. These technologies are not exclusive to EAF operation, but to operations that benefit from increasing the mixing of the molten bath. Among these technologies are electromagnetic stirring (EMS), bottom gas injection (BGI) and injection of oxygen through lances.[3] Applying EMS to a molten bath is an old idea that is not widely applied in the steelmaking industry. Electromagnetic forces, which are normally present in EAF due to electric arcs, can be

enhanced by installing coils at the bottom of the furnace to produce additional stirring on the liquid steel.[4] Recent EMS applications have demonstrated large benefits on decarburization rate during EAF operation.[5] Moreover, BGI can also promote mixing within the molten bath. BGI is extensively applied in ladle operations. However, BGI could lead to the formation of spouts in the liquid surface during EAF operations that would impact negatively on the stability of the electric arc.[3]

The injection of oxygen through lances is widely considered in EAF operations. Namely, lances are placed above the molten steel level in the EAF to inject oxygen. The oxygen injection, which can be produced at supersonic velocities, stirs the liquid bath. Reactions driven by the oxygen injection are key to obtaining the right slag foaming and removing impurities. Oxygen injection also generates bubbles that add additional stirring to the molten bath.[6]

These technologies can enhance the stirring of molten steel and increase the refining performance. However, the optimal parameters of operation must be determined, as these depend on the particular conditions at which the EAF works. Determining optimal parameters of operation requires proper understanding of forces controlling the bath mixing. Extensive research on mixing efficiency has been conducted in channels and serpentine mixers[7–10] as well as in ladles and EAF scenarios. For instance, by using a water model, Zhu et al.[11] determined that tuyeres located off-centric increased mixing in gas-stirred ladles. Results also showed that mixing efficiency is controlled by the angle of blowing. Cheng et al.[12] applied computational fluid dynamics (CFD) tools to study a scaled industrial ladle. This study concluded that side blowing led to shorter mixing times than bottom blowing. Moreover, Li[13] performed computational and experimental analysis of a scaled EAF with bottom stirring to determine the impact of plug parameters on flow mixing. Results showed that mixing is enhanced by off-center blowing of gas and by increasing the number of plugs. On the contrary, it was observed that increasing the diameter of injection plugs has a minor effect on mixing. Still, many questions regarding the mixing process in EAF refining must be clarified in the context of actual EAF operations (both EAF dimensions and operation conditions), since mixing efficiency depends on specific conditions of the system, as concluded from previous research. However, experimental data is very limited in industry-size EAFs, and computational simulations are very difficult to achieve in real-world EAF conditions. Specifically, the presence of coherent jets introduces high-speed regimes, which increase the computational cost of CFD modeling significantly. This makes computational simulations of actual operation (which are in the order of 40–70 minutes) unfeasible. In this study, a CFD solver introduced previously[6] is used to analyze the impact of injection parameters on the refining process. The CFD solver simulates the coherent jets separately from the refining process, and then integrates the coherent jet results into the refining simulation of the molten bath. The CFD simulations consider real-world EAF size and parameters, as provided by EVRAZ. The results are used to determine the impact of oxygen injection on refining performance so that parameters required to optimize the refining process can be established.

Numerical Model

Integrated CFD Simulator for EAF Refining

A CFD platform has been implemented to compute the refining stage of the EAF. CFD implementation is presented in detail in Reference 6. This section contains a brief description of the computational models used to simulate the refining cases of this study. The refining stage is simulated by completing three steps, which are defined based on processes that occur simultaneously during the EAF refining:

- Step 1: Coherent jets are simulated considering injection parameters of actual burners acting in lance mode. This simulation provides velocity and composition of the injecting flow when it reaches the surface of the bath.
- Step 2: Flow parameters obtained in step 1 are used to estimate the cavities produced in the molten steel as a result of oxygen jet impingement.
- Step 3: A CFD domain is generated to simulate molten steel. This domain includes cavities obtained in step 2. A transient simulation is performed, and key reactions of the refining stage are computed. Oxygen is injected through the cavities at the rate provided by the coherent jet solution.

The key equations and mathematical descriptions of steps 1–3 are presented in the next section.

Simulation of the Supersonic Coherent Jet Burners (Steady-State Simulation): The coherent jet injection is computed by using a compressible solver in ANSYS Fluent v2019. In this approach, the continuity equation is given by:

$$\nabla \cdot \left(\rho \vec{v} \right) = 0 \qquad \text{(Eq. 1)}$$

where ρ and $\vec{v}$ are the density and velocity vector, respectively. The momentum equation reads:

$$\nabla \cdot \left(\rho \vec{v}\vec{v} \right) = -\nabla \rho + \nabla \cdot \left(\bar{\bar{\tau}} \right) + \rho \vec{g} + \vec{F} \qquad \text{(Eq. 2)}$$

where ρ, $\bar{\bar{\tau}}$, g and $\vec{F}$ are pressure, stress tensor, gravity acceleration and external body forces, respectively. The energy conservation equation, in turn, reads:

$$\nabla\cdot\left[\vec{v}\left(\rho E+p\right)\right]=\nabla\cdot \left[\left(k+\frac{c_p\cdot\mu_t}{\mathrm{Pr}_t}\right)\nabla T-\sum_j h_j\overrightarrow{J_J}+\left(\bar{\tau}_{eff}\cdot\vec{v}\right)\right]+S_h$$

(Eq. 3)

where

E, k, c_p and μ_t are total energy, thermal conductivity, specific heat, and turbulent viscosity, respectively.

The turbulent Prandtl number Pr_t is 0.85,

$\overrightarrow{J_J}$ is the diffusion flux,

S_h is the heat source.

The $k-\varepsilon$ turbulence model is applied in this study. The turbulence viscosity is calculated by using Eq. 4, along with a constant considered to account for entrainment of ambient gas that is shown in Eq. 5.[14]

$$\mu_t=C_\mu\rho\frac{k^2}{\varepsilon}$$

(Eq. 4)

$$C_\mu=\frac{0.09}{C_T}$$

(Eq. 5)

where C_T is a function of the total temperature of the flow field and turbulent Mach number.

Calculation of the Cavity Produced by the Coherent Jet on Liquid Bath: In the second step, the cavity that the jet impingement would produce on the liquid bath is calculated.[15] The cavity is computed based on the jet momentum and oxygen delivery determined in step 1. The momentum driven by the jet is obtained as follows:

$$P_{s,avg}=\alpha\rho_{O_2}{v_{O_2}}^2A=\frac{\alpha\rho_{O_2}A}{\rho_s}\left[\frac{1}{\Delta z}\int_{z2}^{z1}v_{O_2}\left(z\right)dz\right]^2$$

(Eq. 6)

where α, v_{O_2}, A and Δz are transferable percentage of the jet total momentum at liquid steel bath, which is 0.06,[15] average jet velocity along cavity centerline, cavity surface area and length of cavity centerline, respectively.

The oxygen delivered by the jet to the liquid steel is given by:

$$m_{O_{2,avg}}=\frac{1}{\Delta z}\int_{z2}^{z1}m_{O_2}\left(z\right)dz$$

(Eq. 7)

Due to dampening effects of slag layer and viscosity effects, ~6% of the flow momentum from the jet transfers to the bath.[6] The shape of the cavity is assumed to be a paraboloid determined by:

$$z=\left(\frac{x^2+y^2}{c}\right)$$

(Eq. 8)

where c is determined based on the depth and volume of the cavity. The volume of the cavity is obtained by:[16]

$$V=\frac{\pi\rho_j v_j^2 d_j^2}{4g\rho_s}$$

(Eq. 9)

where

ρ_j and ρ_s are densities of gas jet and liquid steel, respectively.

v_j is jet velocity and

d_j is jet diameter of nozzle.

The depth of the indentation created by the coherent jet in the liquid bath is expressed as:[17]

$$D=\gamma_{h_0}e\frac{\sigma_1 L}{\gamma_{h_0}\cos\theta}$$

(Eq. 10)

$$\gamma_{h_0}=\sigma_2\left(\frac{\dot{V}}{nd\sqrt{3}}\right)$$

(Eq. 11)

where $\dot{V}$, n and d are the volume flow rate of primary oxygen jet, number of nozzles and nozzle exit diameter for primary oxygen jet, respectively. Constants σ_1 and σ_2 are derived from experimental analysis, and are equal to 1.77 and 1.67, respectively.[18]

Stirring of the Bath Due to Jet Injection (Transient Simulation): The third step is the simulation of the liquid steel that would form after all the scrap has melted. The computational model solves a set of incompressible, Eulerian multiphase, Navier-Stokes equations by using

Figure 1

Section of the electric arc furnace (EAF) considered in refining simulations. Cavities produced by burners 1–3 are also indicated.

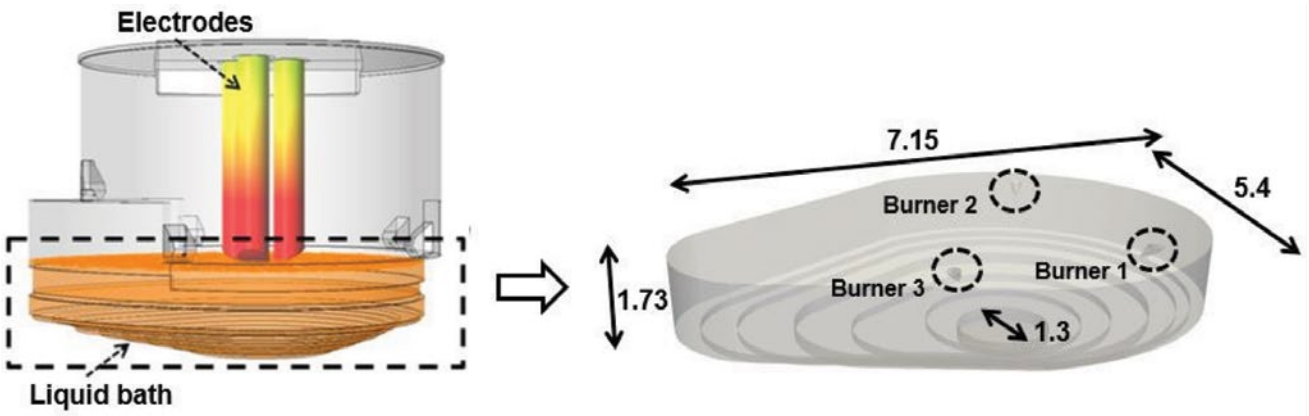

a finite volume scheme in ANSYS Fluent. Here, the primary phase is liquid steel, and the secondary phase is injected oxygen. The computational domain is shown in Fig. 1. Specifically, the CFD domain includes molten steel only and the cavities produced by the oxygen injection.

In addition to the Navier-Stokes equations, a set of decarburization reactions is also computed. These reactions are:

$$C = \frac{1}{2}O_2(g) = CO(g)$$

(Eq. 12)

$$Fe + \frac{1}{2}O_2(g) = FeO$$

(Eq. 13)

$$Mn + \frac{1}{2}O_2(g) = MnO$$

(Eq. 14)

The rate at which these reactions occur is determined as:[19]

$$-\frac{W_S}{100M_{Y_R}}\frac{d[\%Y_R]}{dt} = \frac{2\eta_{Y_R}}{22,400}X_{Y_R}$$

(Eq. 15)

where

W_s and Q_{O_2} are the molten steel mass and oxygen volume in each computational cell and

M_{Y_R}, η_{Y_R} and X_{Y_R} are the mole mass, efficiency factor and oxygen distribution ratios of each substance (Y_R) *C*, *Fe* and *Mn*, respectively.

The oxygen distribution is a function of the Gibbs free energy, namely:

$$X_{Y_R} = \frac{\Delta G_{Y_R}}{\Delta G_C + \Delta G_{Fe} + \Delta G_{Mn}}$$

(Eq. 16)

where the Gibbs free energy is given by:

$$\Delta G_{Y_R} = \Delta G^0_{Y_R} + RT\ln\left[\frac{a_{Y_P}}{a_{Y_R}a_{O_2}^{0.5}}\right]$$

(Eq. 17)

here,

ΔG^0 is the standard Gibbs free energy,

a_{Y_P} is the activity of each substance,

R is the gas constant and

a_Y is the activity of products.

In case the carbon content in the cell is low, however, the rate of oxidation of carbon is not controlled by the available oxygen but by direct mass transfer of carbon to the liquid steel:

$$-W_S\frac{d[\%C]}{dt} = -\rho_S k_C A_{inter}\left([\%C]-[\%C]_e\right)$$

(Eq. 18)

where

A_{inter} is the surface area of the bubble,

$[\%C]_e$ is the carbon equilibrium concentration and

k_C is the mass transfer coefficient, which is $k_C = 0.59\ [D_C (u_{rel}/d_B)]^{0.5}$ as proposed in Reference 20.

Table 1

Parameters Used in the Validation Simulation

Variables	Value
Co-jet quantity	3
Co-jet angle [degrees]	45
O_2 flowrates [scfm]	Burner 1: 1,150 Burner 2: 850 Burner 3: 1,290
Steel liquid density [kg/m^3]	7,500
Steel liquid temperature [K]	1,838 (1,565°C)
C initial content in steel [%]	0.065

Figure 2

Validation results: carbon evolution in time (top) and carbon contours at three selected times (bottom) for validation scenario.

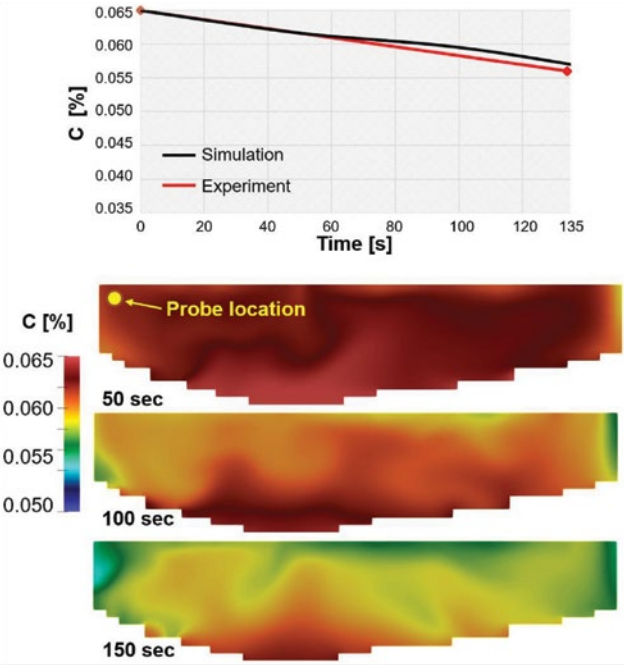

In the expression for k_C, D_C is the diffusion coefficient of carbon, u_{rel} is the relative velocity of the molten steel and d_B is diameter of the bubble. The current CFD approach assumes that products of reactions listed in Eqs. 12–14 are removed from the domain once they reach the top boundary of the domain. This assumption accounts for the mass transfer of oxides from molten steel to slag, which is not directly modeled in the CFD approach. The energy generated in the molten steel due to the oxidation rates are determined by:

$$\frac{dE_{reac}}{dt} = \sum \Delta H_{Y_R} W_S \frac{d\left[\%Y_R\right]}{dt} \quad \text{(Eq. 19)}$$

The CFD domain in the refining simulation has 2.5 million cells. The set of reactions listed in Eqs. 12–19 have been implemented via user-defined functions (UDF). It should be noticed that the CFD domain assumes adiabatic walls and heat exchange between steel and slag is not considered.

Validation

The refining model is validated against a similar refining scenario completed by EVRAZ. The operation conditions of this scenario are shown in Table 1.

Results of validation simulation are shown in Fig. 2. The top of Fig. 2 shows the evolution of carbon content measured by a probe during the refining process. The CFD approach predicts a decarburization of 12.1% after 134 seconds of operation, whereas the experimental value reports 13.8% decarburization within the same time. Therefore, the carbon content prediction differs 1.7% between the two approaches, which can be considered within the experimental error margin. The bottom part of Fig. 2 shows carbon contours at three times, which has been computed in a vertical plane along the centerline of the furnace. Carbon contours show that carbon decays faster at the top of the liquid bath than at the bottom, and the decarburization is enhanced near the walls. The probe location where the carbon data of the top figure was measured is shown in the 50-second contour.

Results and Discussion

Operation Conditions of Case Simulations

The impact of oxygen injection is investigated by completing a set of simulations with conditions similar to those used in actual EVRAZ heats. These cases, however, do not include carbon injection nor arcing, which would be present in EVRAZ operations. The parameter values used in these simulations are listed in Table 2.

The simulations include two main sets of results. The first set considers all the burners injecting oxygen at the same rate during the EAF refining operation. The second

Table 2

Parameters Used in the Case Simulation

Variables	Value
Co-jet quantity	3
Co-jet angle of inclination [degrees]	45
O_2 flowrates [scfm]	750, 1,000, 1,250 scfm (28.2, 37.6, 47 kg/min)
Steel liquid density [kg/m^3]	7,500
Steel liquid temperature [K]	1,890 (1,617°C)
C initial content in steel [%]	0.080

Table 3

Injection Parameters of Cases Considered in This Study

	Oxygen injection [scfm]			
Cases	Burner 1	Burner 2	Burner 3	Total
1	1,000	1,000	1,000	3,000
2	1,250	1,250	1,250	3,750
3	750	750	750	2,250
4	1,250	1,000	750	3,000
5	750	1,250	1,000	3,000
6	1,000	750	1,250	3,000

set considers each of the burners injecting oxygen at a different rate, while keeping the total flowrate the same. Table 3 shows these two sets. The first set is cases 1–3, where case 1 is the baseline case that injects oxygen at 1,000 scfm. Cases 2 and 3 inject oxygen at an increased and at a reduced rate. A second set of cases comprises cases 4–6, where the injection rates have been individually modified while maintaining the total injection rate at 3,000 scfm, as in the baseline case.

Impact of Flowrate on Coherent Jet Flows

As explained earlier, the coherent jet simulation is the first step of the refining modeling. The cases listed in Table 3 consider injection rates of 750, 1,000 and 1,250 scfm. These three oxygen rates are computed, and coherent jet results are shown in Fig. 3. Results show that the flow velocity is maintained along the X/D = 40–50 distance from the burner tip in all the cases. The distance from the tip of the burner to the molten bath surface is X/D = 30, which is indicated by the dashes on the velocity contours. Fig. 3 also compares the axial velocity along the jet centerline for the three injection rates (right side). Results show that axial velocity increases 16% when the oxygen rate is increased from 1,000 to 1,250 scfm, and reduces 30% when the oxygen rate is decreased from 1,000 to 750 scfm.

Impact of Injection Rate on Cavities Forming on Surface Bath

The second part of the CFD modeling is to calculate the cavities that the coherent jets produce on the molten steel surface. Following the procedure described earlier, the cavity depth and volume is obtained for the 750, 1,000 and 1,250 scfm injection cases. The cavity size increases with injection rate as seen in Fig. 4. Specifically, the cavity volume increases 27.8% when increasing the oxygen rate 25% from baseline 1,000 scfm and reduces 25% when the oxygen injection is decreased 25% from the baseline injection condition. These cavities are then included in

Figure 3

Injection of oxygen driven by coherent jets operating in lance mode for the three injection rates considered in this study.

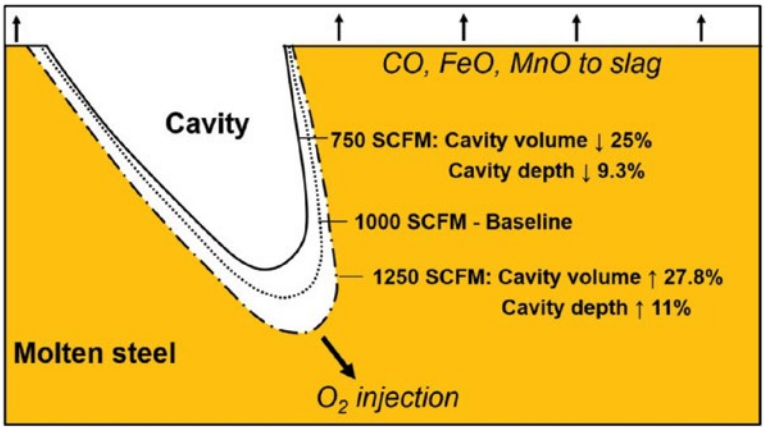

Figure 4

Cavity formed due to jet impingement on liquid bath for the three injection rates considered in this study.

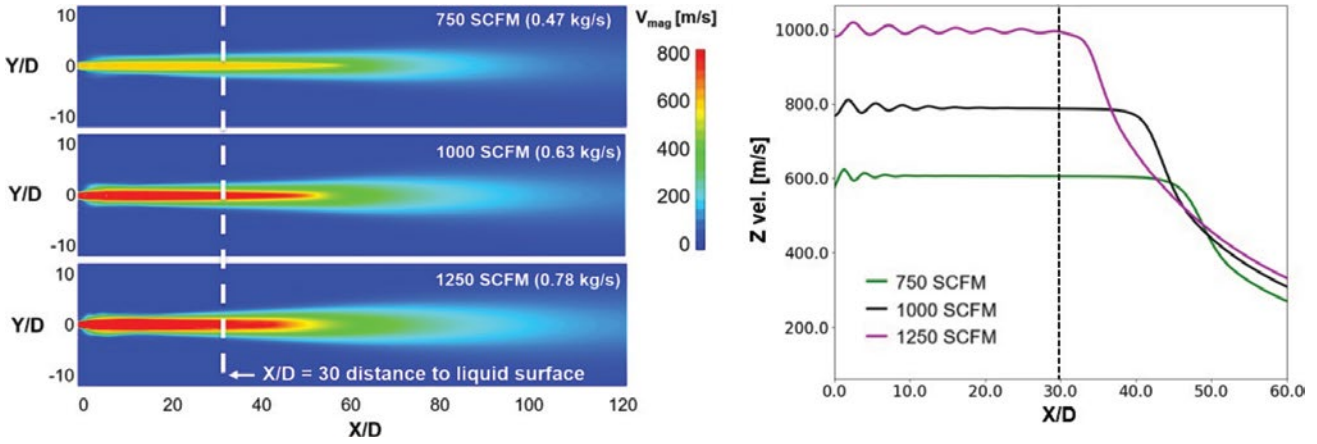

the CFD setup of the refining simulation as part of the computational grid.

Baseline Results in Steel Bath Domain

The third part of the CFD modeling simulates the liquid steel and oxygen injection through the cavities obtained in the second step. The baseline case considers oxygen injected at 1,000 scfm in all burners (case 1 in Table 3). Results with baseline injection are shown in Fig. 5. Specifically, liquid temperature and velocity magnitude of the liquid steel are computed in a plane near the surface of the steel bath. The largest steel temperatures are seen near burners 1 and 3, as well as at the slag door, where burners 1 and 2 are located. In the center of the plane, low-temperature regions form and extend toward the balcony. These temperature contours are related to the flow field, since the larger flow velocities are seen near burners 1 and 3 as well. The flow vectors show flow recirculation near the cavities, and low liquid velocities at the balcony. Overall, the flow velocities are in the 0.1–0.5 m/second range in this plane. The flow velocities decay away from the cavities formed in the surface of the bath, where the velocities reach up to 5–7 m/second. The flow and temperature fields show nonuniform features, where large gradients can be observed locally. The lowest velocities and liquid temperatures are seen at the center of the domain and at the balcony. These features are enhanced by the asymmetric shape of the furnace and distribution of the burners, which enhance local variations.

Figure 5

Liquid temperature and velocity field for baseline case.

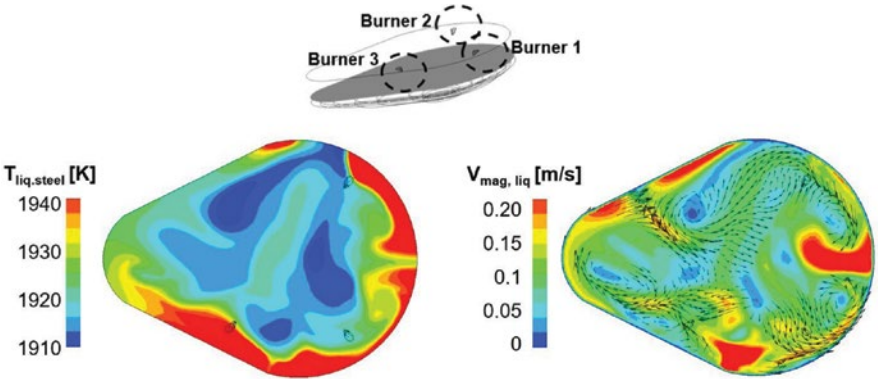

The evolution of the carbon content and temperature of the liquid bath is shown in Fig. 6. The carbon content and liquid temperature values are mass-integrated throughout the liquid region. The carbon reduces from the initial 0.08% as the refining reactions take place. The refining reactions also lead to the increase of the bath temperature. The carbon content reduces 20% after 5 minutes of operation. In this time, the bath temperature increases 33 K from the initial bath temperature set at 1,890 K.

Impact of Uniform Increasing and Decreasing of Oxygen Injection

The baseline case, where all burners inject oxygen at 1,000 scfm, is compared to two cases where the injection rates are reduced to 750 scfm and increased to 1,250 scfm,

Figure 6

Carbon and temperature evolution for baseline case along refining operation.

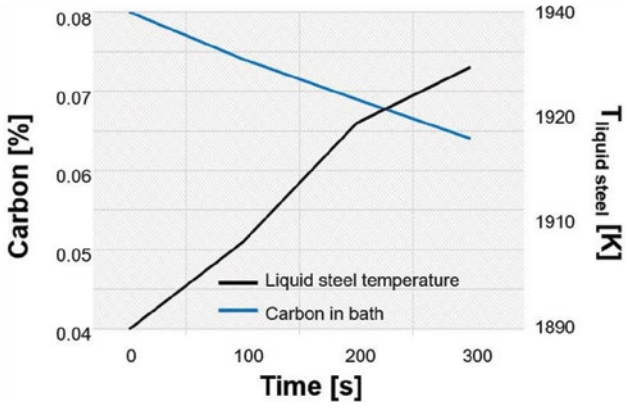

Figure 7

Comparison of flow fields obtained with baseline, reduced (750 scfm) and increased (1,250 scfm) oxygen injection cases.

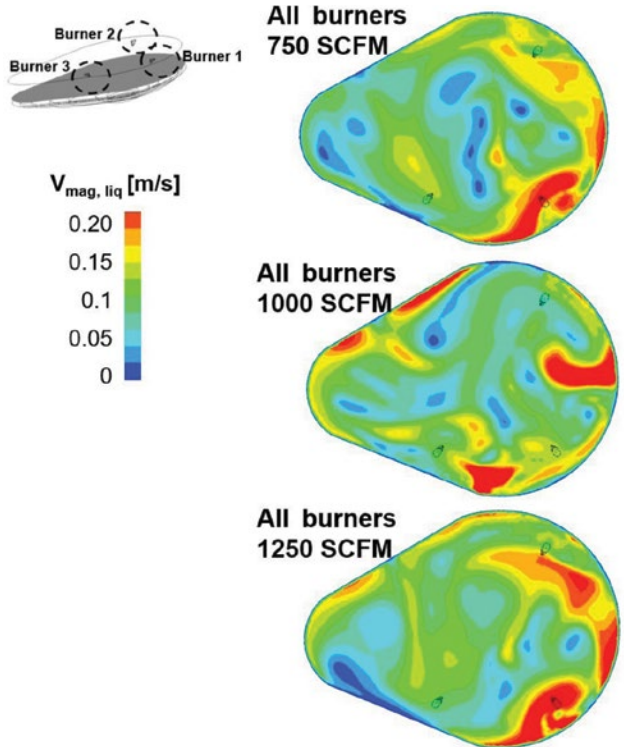

respectively. The reduced and increased injection rate cases confirm the flow features seen in the baseline case. Namely, large velocity regions are seen at the walls of the furnace near burners 1, 2 and 3, whereas low velocities are formed at the center of the furnace and at the balcony for all the cases (Fig. 7). As expected, the increased injection rates lead to larger flow velocities in the liquid bath. In the 1,250 scfm case, it is possible to see increased flow velocities in the center of the furnace as compared to 750 and 1,000 scfm injection cases.

Increased flow velocities achieved by increasing the injection rates have an impact on the decarburization rate of the liquid steel bath. Namely, Fig. 8 shows that carbon content in the liquid bath reduces 15% when burners inject oxygen at 750 scfm during the first 300 seconds of operation. These increase to 20% by increasing the flow to 1,000 scfm and to 25% when the oxygen injection is further increased to 1,250 scfm. Similarly, the bath temperature is increased as the carbon reduction is enhanced (shown on the right side of Fig. 8). Specifically, the bath temperature raises 8 K when the injection rate is

Figure 8

Evolution of carbon content and temperature of molten steel for baseline, increased and reduced oxygen injection rates.

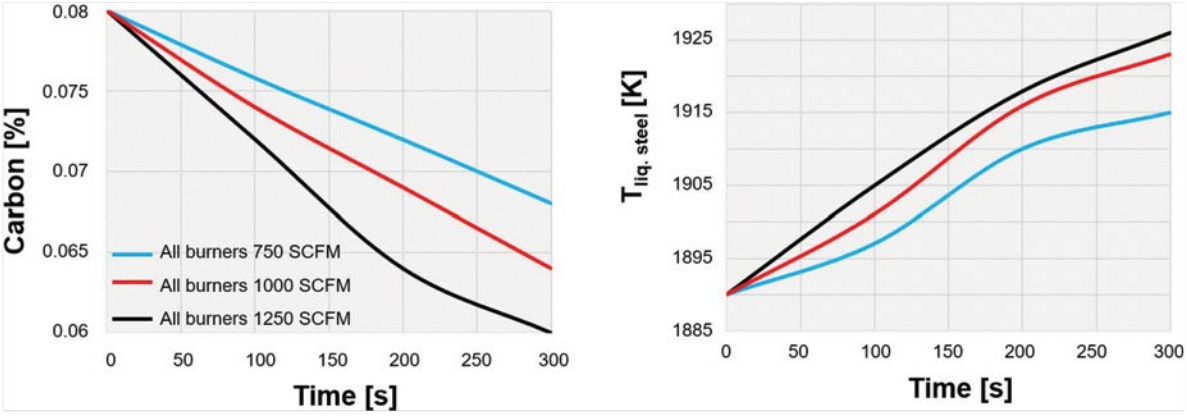

Figure 9

Comparison of flow fields obtained with baseline and individually modified injection rates.

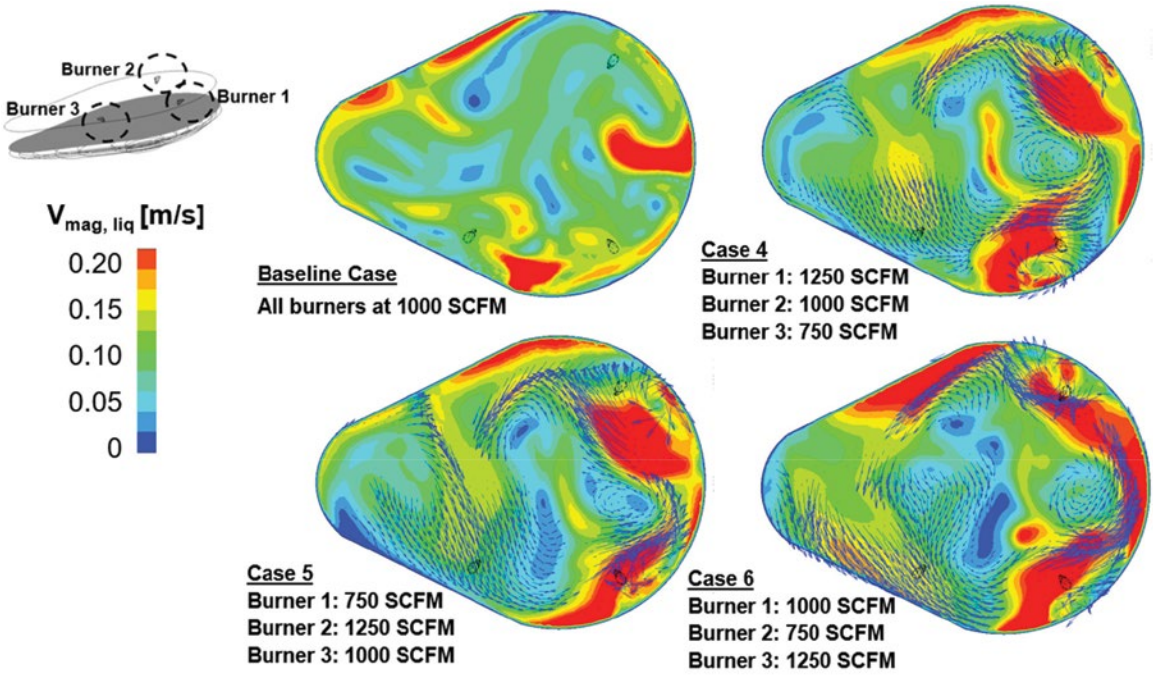

Figure 10

Evolution of carbon content and temperature of molten steel for baseline and individually modified oxygen injection rates.

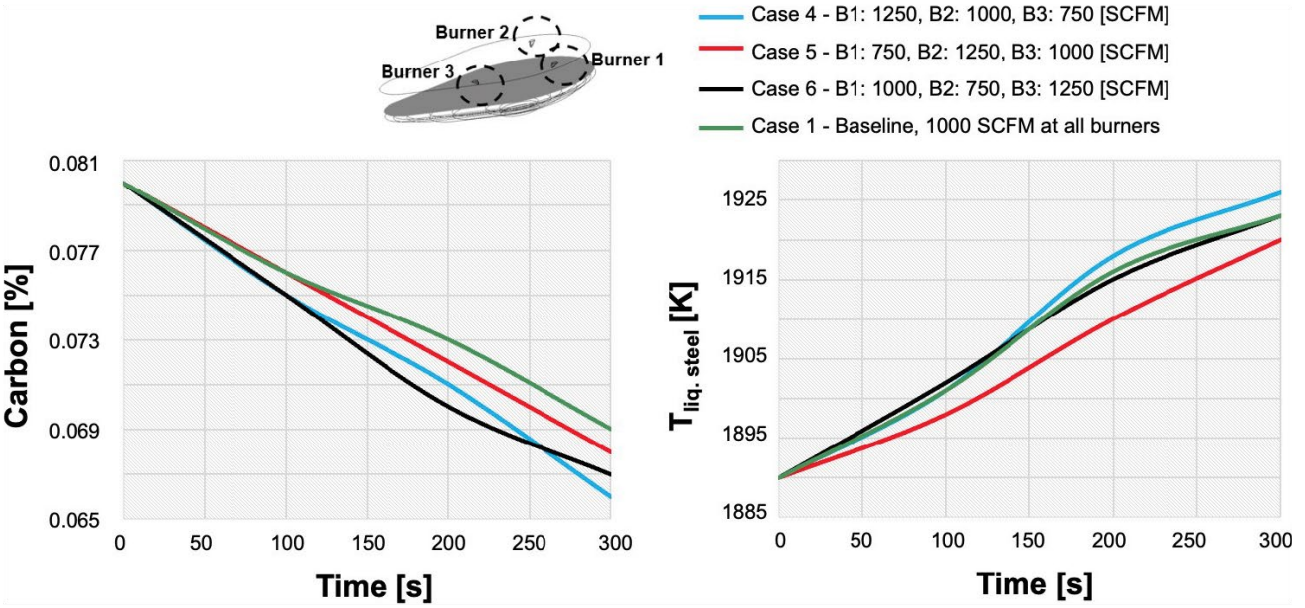

increased from 750 to 1,000 scfm, and 3 K when the baseline injection rate is increased to 1,250 scfm. Although the injection rate has a consistent impact of increasing the liquid temperature, this increasing is minor, and it would be within the error range seen in an experimental study.

Impact of Varying Oxygen Injection in Each Burner

This section discusses three additional cases where the oxygen rate in each burner is modified, cases 4–6. These cases and the baseline case have the same total injection rate, 3,000 scfm. It is expected that by modifying the injection rate at each burner, the nonuniformity of the flow is promoted and the mixing enhanced. Fig. 9 shows the results of the baseline and cases 4–6. All cases with individually modified injection led to larger flow velocities than the baseline case. Case 6 increases the liquid velocity even at the balcony region. However, case 6 also increases the low-velocity regions seen at the center of the furnace. These low-velocity regions or "dead zones" are reduced in case 4, where the larger injection rates are provided by burners located near the slag door.

The individually modified injection cases have an impact on the decarburization rate. Namely, Fig. 10 shows that case 4 decreases the carbon content 17.5% at the end of 300 seconds of refining operation. The baseline case reduces carbon 13.7% within the same operation time. Therefore, an additional 3.75% reduction is achieved by modifying the injection rate of the burners while maintaining the same total injection. Among the three cases with individually modified injection rates, case 4 shows the better decarbonization rate. Case 4 also leads to the largest increase of bath temperature. As seen in Fig. 10 (right), molten steel temperature increases 36 K in this case, as compared with the 30 K increase seen in the baseline case. It should be noted that case 4 does not show the largest flow velocities in the furnace, but it leads to the smallest region of low velocities or dead zones. As mentioned earlier, the total oxygen injection is the same in these cases, but the modified injection rate distributions in the furnace lead to the changes seen in the decarburization efficiency.

Conclusions

This study uses a CFD platform that has been developed to compute the refining stage in an industry-scale EAF. The CFD solver uses three steps: simulation of the coherent jets, computation of the cavities produced by coherent jets on the liquid bath and simulation of the molten steel as oxygen is injected at these cavities. This approach prevents modeling of high-speed regimes driven by coherent jets during refining, which makes CFD simulations of real-world refining processes feasible.

The industry-size EAF considered in this study is provided by EVRAZ. This includes three burners, which are placed in an asymmetrical arrangement. A validation analysis is first performed, where CFD predictions of decarburization process differ 1.7% from actual data provided by EVRAZ. The impact of oxygen injection is then studied by varying the injection parameters and analyzing the refining performance in each of these scenarios. Since the velocity and thermal gradient control the reaction rates, it is expected that refining performance can be enhanced by promoting flow mixing. A baseline case is computed by assuming the same oxygen rate in each burner at 1,000 scfm. This case is then compared with two cases where the injection rate is increased to 1,250 scfm and reduced to 750 scfm. From these three cases, the following can be concluded:

- The baseline case shows that high liquid steel temperature develops at the walls near the burners, and cold spots form in the center of the domain and at the balcony region. The liquid velocity field correlates to the temperature field by showing the larger velocities in the same regions of large molten steel temperatures.
- By increasing and reducing the oxygen injection, the flow pattern does not change significantly as compared to the baseline case, but the velocity magnitudes vary with the injection rate. In all cases, the velocities are large near the slag door and low-velocity regions on dead zones form in the center of the domain.
- The injection rate impacts the decarburization rate obtained during the refining. In particular, it is seen that the carbon content decreases 25% when oxygen is injected at 1,250 scfm. This improves the decarburization rate seen in the baseline case by 5%.

A second set of simulations is completed where the oxygen injection in each of the burners is modified, while maintaining the total injection rate the same as the baseline case, 3,000 scfm. From these cases, the following can be concluded:

- The flow patterns resemble those obtained in the baseline case. Namely, the largest flow velocities are seen near the slag door and dead zones form in the central region of the furnace.
- The dead zone regions are reduced when the largest injection rates are produced near the slag door. In this case, the decarburization rate increases 3.75% with respect to the baseline case. This is the largest improvement seen among the nonuniform oxygen injection cases.

Acknowledgments

The authors would like to thank the members of the Steel Manufacturing Simulation and Visualization Consortium for their support and consultation on this research. The authors would also like to thank the staff and students at Purdue University Northwest's Center for Innovation Through Visualization and Simulation for their support and for the resources to conduct this research.

This article is available online at AIST.org for 30 days following publication.

References

1. Z. Fan and S.J. Friedmann, "Low-Carbon Production of Iron and Steel: Technology Options, Economic Assessment, and Policy," *Joule,* Vol. 5, No. 4, 2021, pp. 829–862.
2. T. Puschmann, C.H. Hoffmann and V. Khmarskyi, "How Green FinTech Can Alleviate the Impact of Climate Change — The Case of Switzerland," *Sustainability,* Vol. 12, 2020.
3. N. Conejo and Y. Zhaozhao, "Electric Arc Furnace Stirring: A Review," *Steel Research International,* Vol. 94, No. 7, 2023.
4. L. Dreyfus, U.S. Patent 2256518, 1941.
5. L. Teng, M. Meador and P. Ljungqvist, "Application of New Generation Electromagnetic Stirring in Electric Arc Furnace," *Steel Research International,* Vol. 88, No. 4, 2017.
6. Y. Chen, A.K. Silaen and C.Q. Zhou, "3D Integrated Modeling of Supersonic Coherent Jet Penetration and Decarburization in EAF Refining Process," *Processes,* Vol. 8, 2020, p. 700.
7. S. Jayaraj, S. Kang and Y.K. Suh, "A Review on the Analysis and Experiment of Fluid Flow and Mixing in Micro-Channels," *J. Mech. Science Tech.,* Vol. 21, 2007, pp. 536–548.
8. T.G. Kang and P.D. Anderson, "The Effect of Inertia on the Flow and Mixing Characteristics of a Chaotic Serpentine Mixer," *Micromachines,* Vol. 5, 2014, pp. 1270–1286.
9. R.H. Liu, M.A. Stremler, K.V. Sharp, M.G. Olsen, J.G. Santiago, R.J. Adrian, H. Aref and D.J. Beebe, *J. Microelectromech. Syst.,* Vol. 9, 2000, pp. 190–197.
10. E. Lang, P. Drtina, F. Streiff and M. Fleischli, "Numerical Simulation of the Fluid Flow and the Mixing Process in a Static Mixer," *Int. J. Heat Mass Transfer,* Vol. 38, 1995, pp. 2239–2250.
11. M.Y. Zhu, T. Inomoto, I. Sawada and T.C. Hsiao, "Fluid Flow and Mixing Phenomena in the Ladle Stirred by Argon Through Multi-Tuyere," *ISIJ Int.,* Vol. 35, 1995, pp. 472–479.
12. R. Cheng, L. Zhang, Y. Yin and J. Zhang, "Effect of Side Blowing on Fluid Flow and Mixing Phenomenon in Gas-Stirred Ladle," *Metals,* Vol. 11, 2021, p. 369.
13. B. Li, "Fluid Flow and Mixing Process in a Bottom Stirring Electrical Arc Furnace With Multi-Plug," *ISIJ Int.,* Vol. 40, 2000, pp. 863–869.
14. G. Tang, Y. Chen, A.K. Silaen, Y. Krotov, M.F. Riley and C.Q. Zhou, "Investigation on Coherent Jet Potential Core Length in an Electric Arc Furnace," *Steel Res. Int.,* Vol. 90, 2019.
15. M. Sano and K. Mori, "Fluid Flow and Mixing Characteristics in a Gas-stirred Molten Metal Bath," *Trans. Iron Steel Inst. Jpn.,* Vol. 23, 1983, pp. 169–175.
16. R.B. Banks and D.V. Chandrasekhara, "Experimental Investigation of the Penetration of a High-Velocity Gas Jet Through a Liquid Surface," *J. Fluid Mech.,* Vol. 15, 1963, pp. 13–34.
17. H. Ishikawa, S. Mizoguchi and K. Segawa, "A Model Study on Jet Penetration and Slopping in the LD Converter," *ISIJ Int.,* Vol. 58, 1972, pp. 76–84.
18. O.J.P. Gonzalez, M.A. Ramírez-Argáez and A.N. Conejo, "Effect of Arc Length on Fluid Flow and Mixing Phenomena in AC Electric Arc Furnaces," *ISIJ Int.,* Vol. 50, 2010, pp. 1–8.
19. J.H. Wei and D.P. Zhu, "Mathematical Modeling of the Argon-Oxygen Decarburization Refining Process of Stainless Steel: Part I. Mathematical Model of the Process," *Metall. Mater. Trans. B,* Vol. 33, 2002, pp. 111–119.
20. H. Saint-Raymond, D. Huin and F. Stouvenot, "Mechanisms and Modeling of Liquid Steel Decarburization Below 10 ppm Carbon," *Mater. Trans. JIM,* Vol. 41, 2000, pp. 17–21.

AISTech This paper was presented at AISTech 2024 — The Iron & Steel Technology Conference and Exposition, Columbus, Ohio, USA, and published in the AISTech 2024 Conference Proceedings.